



Article

# Two-Step Exfoliation of WS<sub>2</sub> for NO<sub>2</sub>, H<sub>2</sub> and Humidity Sensing Applications

Valentina Paolucci <sup>1,\*</sup>, Seyed Mahmoud Emamjomeh <sup>1</sup>, Michele Nardone <sup>2</sup>, Luca Ottaviano <sup>2,3</sup> and Carlo Cantalini <sup>1</sup>

<sup>1</sup> Department of Industrial and Information Engineering and Economics, Via G. Gronchi 18, University of L'Aquila, I-67100 L'Aquila, Italy; seyedmahmoud.emamjomeh@graduate.univaq.it (S.M.E.); carlo.cantalini@univaq.it (C.C.)

<sup>2</sup> Department of Physical and Chemical Sciences, Via Vetoio 10, University of L'Aquila, I-67100 L'Aquila, Italy; michele.nardone@univaq.it (M.N.); luca.ottaviano@aquila.infn.it (L.O.)

<sup>3</sup> CNR-SPIN Uos L'Aquila, Via Vetoio 10, I-67100 L'Aquila, Italy

\* Correspondence: valentina.paolucci2@graduate.univaq.it

Received: 30 August 2019; Accepted: 17 September 2019; Published: 24 September 2019



**Abstract:** WS<sub>2</sub> exfoliated by a combined ball milling and sonication technique to produce few-layer WS<sub>2</sub> is characterized and assembled as chemo-resistive NO<sub>2</sub>, H<sub>2</sub> and humidity sensors. Microstructural analyses reveal flakes with average dimensions of 110 nm, “aspect ratio” of lateral dimension to the thickness of 27. Due to spontaneous oxidation of exfoliated WS<sub>2</sub> to amorphous WO<sub>3</sub>, films have been pre-annealed at 180 °C to stabilize WO<sub>3</sub> content at ≈58%, as determined by X-ray Photoelectron Spectroscopy (XPS), Raman and grazing incidence X-ray Diffraction (XRD) techniques. Microstructural analysis repeated after one-year conditioning highlighted that amorphous WO<sub>3</sub> concentration is stable, attesting the validity of the pre-annealing procedure. WS<sub>2</sub> films were NO<sub>2</sub>, H<sub>2</sub> and humidity tested at 150 °C operating Temperature (OT), exhibiting experimental detection limits of 200 ppb and 5 ppm to NO<sub>2</sub> and H<sub>2</sub> in dry air, respectively. Long-term stability of the electrical response recorded over one year of sustained conditions at 150 °C OT and different gases demonstrated good reproducibility of the electrical signal. The role played by WO<sub>3</sub> and WS<sub>2</sub> upon gas response has been addressed and a likely reaction gas-mechanism presented. Controlling the microstructure and surface oxidation of exfoliated Transition Metal Dichalcogenides (TMDs) represents a stepping-stone to assess the reproducibility and long-term response of TMDs monolayers in gas sensing applications.

**Keywords:** 2D-materials; WS<sub>2</sub>; exfoliation; gas sensors; NO<sub>2</sub>; H<sub>2</sub>; cross sensitivity

## 1. Introduction

In recent years, layered materials such as two-dimensional (2D) transition metal dichalcogenides (TMDs) have attracted a high level of interest due to their features, which make them appealing for potential applications in gas sensing [1,2], photo-electro-catalytic hydrogen evolution [3,4] optical and electronic devices [5,6] and energy storage [7,8].

Few-layer 2D TMDs can be produced through different methodologies like mechanical and liquid phase exfoliation of bulk crystals, classified as top-down routes, or via direct bottom-up routes like chemical vapor deposition [9,10]. High-yield liquid exfoliation methods comprising ion intercalation [11,12] and ultrasonic cleavage [13,14] have also been widely employed to exfoliate bulk-layered materials. Besides liquid phase exfoliation, low energy ball milling as a newly explored high-yield mechanical exfoliation method has been utilized for scalable production of mono and few-layer graphene [15,16] and TMDs nano-sheets [17,18]. More recently, enhanced mixed methods

comprising assisted grinding and sonication have been shown to produce higher concentrations of TMDs nano-sheets and a reduced amount of defects [19].

Regarding gas sensing applications, 2D single layer MoS<sub>2</sub> Field Effect Transistor [20,21] Pd-doped WS<sub>2</sub> films [22] have been shown to be alternative substitutes for traditional metal oxides sensors. Moreover, considering that the possibility to find practical applications of those materials is generally dependent on the reproducibility of the preparation with respect to both microstructure (i.e., number of layers, lateral size, surface area, etc.) and chemical composition (i.e., defects concentration and surface oxidation), the need to find a practical, high-reproducible, and easy way to exfoliate TMDs is always under investigation. We already presented the fabrication of chemo-resistive thin films gas sensor, by drop casting suspensions of few flakes graphene oxide [23], phosphorene [24] and more recently TMDs utilizing both liquid-exfoliated MoS<sub>2</sub> [25] and commercially exfoliated suspensions of WS<sub>2</sub> [26]. The aim of this work is to apply a low energy ball milling and sonication method to achieve a reproducible and high-yield exfoliation methodology and to test the gas sensing performances of the obtained material. Starting from commercial WS<sub>2</sub> powders, we have firstly performed the exfoliation process based on the grinding and sonication method and investigated the morphology of few flakes WS<sub>2</sub>. Secondly, we have determined that with exposing the material to mild air annealing at 180 °C, a controlled partial oxidation of WS<sub>2</sub> flakes to amorphous WO<sub>3</sub> is achievable. Lastly, we investigated the sensing responses to NO<sub>2</sub>, H<sub>2</sub> and humidity of drop casted exfoliated WS<sub>2</sub> chemo-resistive thin films, discussing the likely gas-response mechanism.

## 2. Materials and Methods

*WS<sub>2</sub> exfoliation:* According to the flow sheet shown in Supplementary Figure S1, 2 g of WS<sub>2</sub> commercial powder (Sigma–Aldrich 243639-50G, St. Louis, MO, USA) were dispersed in 4 mL Acetonitrile (ACN—VWR 83639.320, Radnor, PA, USA) with 30 g Zirconium Oxide balls (D = 3 mm), and ball milled in a planetary milling machine (Fritsch—Planetary Micro Mill Pulverisette 7, Idar-Oberstein, Germany) at 400 rpm, for 2 h in ambient air.

To evaporate ACN residuals after milling, the collected slurry was left overnight at 23 ± 2 °C temperature and 40% ± 3% Relative Humidity (RH) (ATP DT-625 High Accuracy Thermo-hygrometer, Ashby-de-la-Zouch, UK). After ACN evaporation, 0.05 g of the dried powder was dispersed in 100 mL of pure ethanol (99.94% VWR 20821.330, Radnor, PA, USA) and probe sonicated (Sonics VC 505 ultrasonic processor, Newtown, CT, USA) at 250 W for 90 min in a thermostat bath to prevent temperature rise (T 25 °C). Finally, the solution was centrifuged at 2500 rpm for 40 min in a refrigerated (20 ± 2 °C) micro-centrifuge (Eppendorf 5417R, Hamburg, Germany) and the supernatant collected.

*Microstructural and chemical characterization:* Air tapping mode Atomic Force Microscopy (AFM) was performed with a Veeco Digital D5000 system. Using silicon tips with spring constant of 3 N·m<sup>-1</sup> and resonance frequencies between 51 and 94 kHz. Samples for AFM investigations were prepared via spinning (at 2000 rpm for 30 s) 10 µL of centrifuged WS<sub>2</sub>/Ethanol solution on a Si<sub>3</sub>N<sub>4</sub> substrate. The substrates have been previously cleaned in a piranha base solution (3:1:3 mixture of ammonium hydroxide NH<sub>4</sub>OH with hydrogen peroxide and milli-Q water) to enhance their wettability.

Exfoliated flakes were investigated using High Resolution Transmission Electron Microscopy HRTEM—JEOL 2100 Field Emission electron microscope (Tokyo, Japan) operated at 200 kV. Samples prepared by drop casting the WS<sub>2</sub>/Eth solution on Si<sub>3</sub>N<sub>4</sub> substrate were investigated by X-Ray Photoelectron Spectroscopy (XPS) using a PHI 1257 spectrometer (Perkin Elmer, Norwalk, CT, USA) equipped with a monochromatic Al Kα source (hν = 1486.6 eV) with a pass energy of 11.75 eV (93.9 eV survey), corresponding to an overall experimental resolution of 0.25 eV. Raman spectra were acquired using a Micro Raman Spectrometer (µRS) (LABRAM spectrometer, λ = 633 nm, 1 µm spatial resolution, and ≈2 cm<sup>-1</sup> spectral resolution, Horiba-Jobin Yvon, Kyoto, Japan) equipped with a confocal optical microscope (100 × MPLAN objective with 0.9 numerical aperture and 0.15 mm work distance). 10 µL of the WS<sub>2</sub>/Eth solution was deposited on a 270 nm SiO<sub>2</sub> substrate.

*Gas sensing measurements:* Electrical properties were determined by a volt-amperometric technique (AGILENT 34970A), as reported in Supplementary Figure S2, utilizing WS<sub>2</sub> thin films prepared by multiple drop casting and air annealing at 180 °C for 1 h the centrifuged WS<sub>2</sub>/Eth suspension on Si<sub>3</sub>N<sub>4</sub> substrates provided with 30 μm-spaced Pt interdigitated electrodes on the front side and a Pt resistor acting as a heater on the back side. Different gas concentrations in the range 1 ppm–250 ppm H<sub>2</sub> and 40 ppb–5 ppm NO<sub>2</sub> were obtained by mixing certified H<sub>2</sub>, and NO<sub>2</sub> mixtures with dry air carrier, by means of an MKS147 multi gas mass controller. Different relative humidity (RH) air streams in the 10–80% RH range were obtained by mixing dry with saturated water-vapor air. The following definitions apply to discuss the gas response properties: base line resistance (BLR): the resistance in dry air at equilibrium before gas exposure, relative response (RR): the ratio ( $R_A/R_G$ ) where  $R_A$  represents the resistance in air and  $R_G$  the one in gas at equilibrium for a given gas concentration, and sensor sensitivity (S): is the slope of the calibration curve in the sensitivity plot.

### 3. Results and Discussion

#### 3.1. Microstructural Properties of Exfoliated WS<sub>2</sub>

The microstructure of exfoliated WS<sub>2</sub> obtained by the combined ball milling and sonication process is characterized. In our case, acetonitrile (ACN) as the milling solvent, with surface tension of 29.5 mJ m<sup>-2</sup> [27], has been selected as a trade-off between surface tension and moderate boiling point, enabling complete removal of the solvent at room temperature after grinding.

Regarding the influence of the grinding time, particles' size distribution of the starting WS<sub>2</sub> powder (blue plot), determined by Dynamic Light Scattering (DLS) technique (see experimental section) and shown in Figure 1a, downshifts towards smaller average sizes after 72 h grinding (red plot) and slightly further after 90 min sonication (green plot). The particle size distribution of the WS<sub>2</sub> starting powder displays an average particle size of ≈ 8 μm (blue plot) whereas the 72 h ball milled shows a bimodal distribution (red plot), with larger aggregates centered at ≈ 20 μm and smaller ones at ≈ 0.7 μm. After 90 min sonication, the bimodal distribution of the grinded powder disappears (green plot) and the average particle dimension places at ≈ 0.6 μm.

It may be concluded that grinding has an effective influence to reduce the particle size, while sonication, beside its effectiveness to suppress the bimodal distribution (presumably by separating agglomerated WS<sub>2</sub> particles), shows only minor effects to further decrease the particle size of the grinded powder, confirming the dominant role of the milling step. Figure 1b shows the AFM image of the 72 h ball milled and 90 min sonicated WS<sub>2</sub> sample. The inset of this image depicts a rough thickness profile along the selected line, with an average height from the substrate of 2 nm. Low and high magnification TEM images illustrated in Figure 1c,d, show that long term ball milling for 72 h results in a fragmented structure, which was eventually revealed to be amorphous by fast Fourier electron diffraction measurements. These features can be explained considering the two main forces induced by ball milling. The primary force is the shear force provided by rolling of balls on the surface of layers, which causes the removal and the exfoliation of surface layers. The secondary force is the vertical impact from the balls which combined with longer grinding times can fragment the larger exfoliated sheets into smaller ones, eventually collapsing of the crystal structure [15,28].

With the aim to minimize the fragmentation effect, we have reduced the ball milling duration time from 72 to 2 h, maintaining the sonication time at 90 min. Decreasing the milling time to 2 h, the flake's fragmentation sharply decreases, enforcing the formation of well-defined terraced structures comprising stacked WS<sub>2</sub> flakes, as shown in Figure 1e,f.

Figure 2 shows the main microstructural features of the 2 h ball milled and 90 min sonicated WS<sub>2</sub> powders. The AFM image shown in Figure 2a depicts the formation of a well-shaped 2D-flake with a large flat surface of 1 μm length. The corresponding thickness profile drawn in Figure 2b highlights a clear formation of a stacked structure comprising a 3 nm thick basal plane, 6 nm thick secondary plane and a third one at the top. Considering that the slight step on top of the profile,

0.6 nm high, corresponds to 1 layer thickness  $WS_2$  [29], it is shown that the first step is made of 5 layers and the second one of 10 layers, respectively. The 2D character of the actual stacked structure shown in Figure 2b, as defined by the “aspect ratio” (i.e., the ratio of lateral dimension to the thickness), is high, with an associated value of 250, attesting to the successful optimization of the grinding time for exfoliation. The low-resolution TEM image depicted in Figure 2c also illustrates a well-shaped exfoliated flake with edge angles of  $120^\circ$ , confirming the preservation of the typical crystalline  $WS_2$  hexagonal geometry.

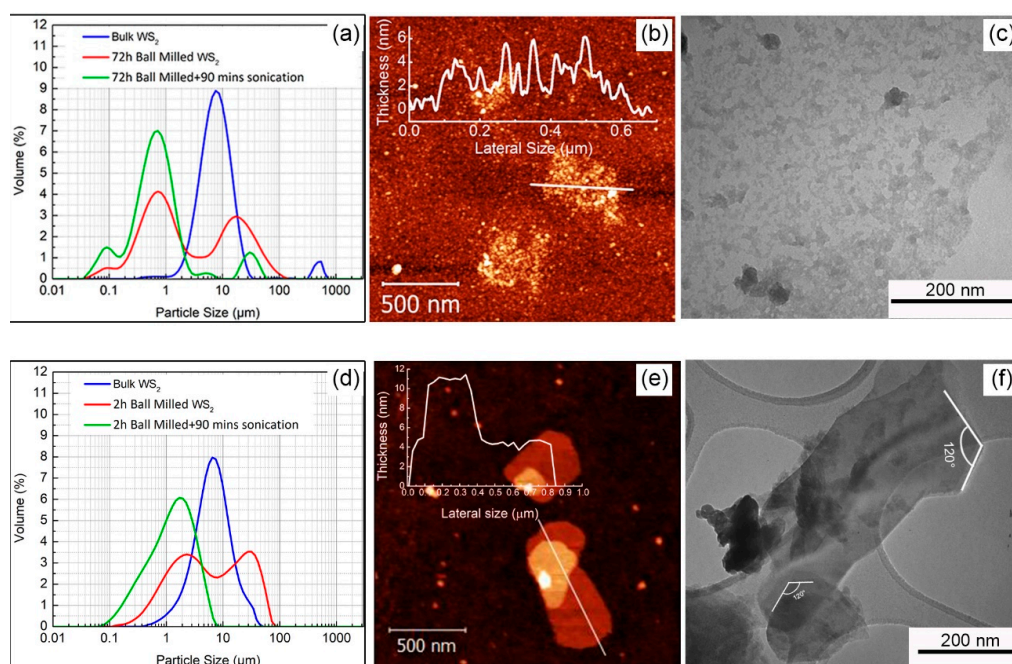


**Figure 1.** Comparison of the effect of long-time ball milling on  $WS_2$  exfoliation: (a) Comparison of the particle size distribution of the starting  $WS_2$  commercial powder (blue), 72 h ball milled (red) and 72 h ball milled and 90 min sonicated (green), (b) AFM picture of 72 h ball milled and 90 min sonicated and associated thickness profile along the white line, (c) TEM picture of the 72 h ball milled and 90 min sonicated  $WS_2$ , (d) Comparison of the particle size distribution in case of 2 h ball milling, (e) AFM picture of 2 h ball milled and 90 min sonicated and associated thickness profile, (f) TEM picture of the flakes obtained by 2 h ball milling and 90 min sonication of  $WS_2$ .

Figure 3 shows HRTEM images of both edges and surfaces of the flakes. Figure 3b (the magnification of Figure 3a), exhibits two layers with associated interlayer distances of  $\approx 0.63$  nm which is in good agreement with the AFM thickness measurements illustrated in Figure 2b. This interlayer displacement could also be observed at the flake’s edges depicted in Figure 3d, where almost 11 layers can be clearly counted on the 7 nm thick edge. The atoms arrangement displayed in Figure 3b exhibits the hexagonal atomic structure, with lattice spacing of 0.27 nm and 0.25 nm, that are characteristics of (100) and (101) crystal planes of 2H- $WS_2$  flakes, respectively [30,31]. Moreover, the Fast Fourier Transforms (FFTs) shown as the inset of Figure 3d, further confirms the hexagonal crystalline structure of the flake.

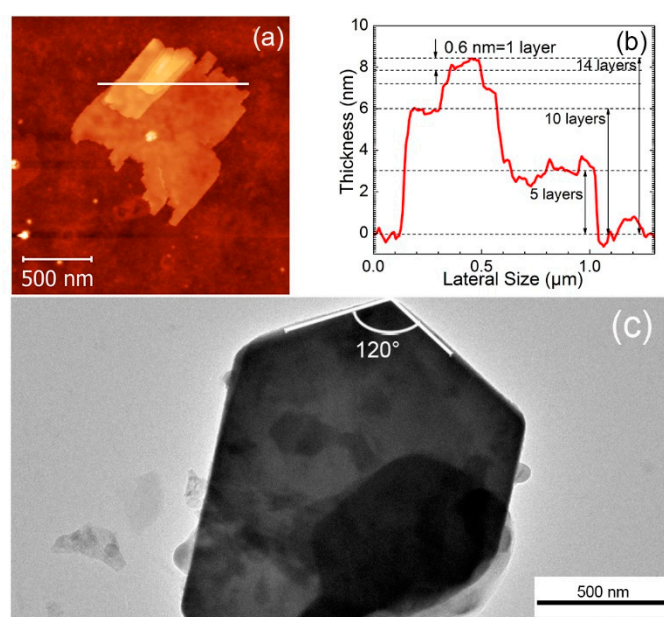


**Figure 2.** (a) AFM picture of the 2 h ball milled and 90 min sonicated  $WS_2$ , (b) thickness profile of the stacked flake along the white line of Figure (a), (c) low-resolution TEM picture of an exfoliated flake.

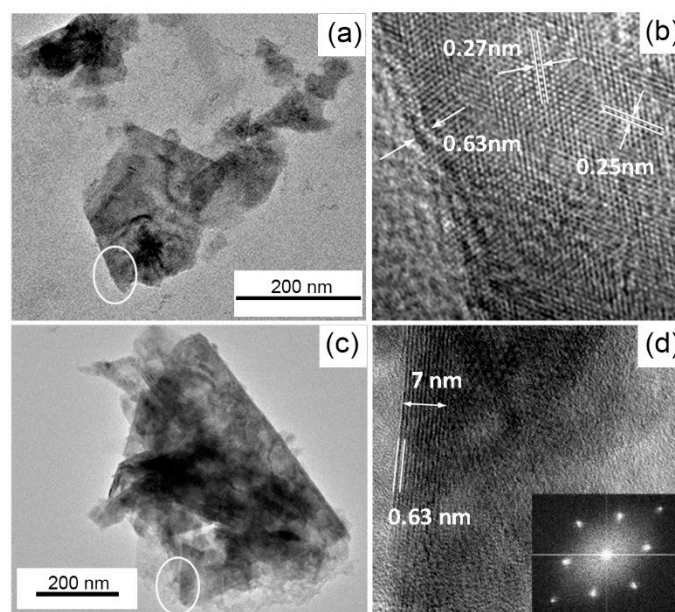


**Figure 3.** (a,c) TEM of 2 h ball milled and 90 min sonicated  $WS_2$ , (b) HRTEM corresponding to the circled area shown in figure (a) with highlighted the interlayer distance (0.63 nm) and lattice spacing (0.27 nm and 0.25 nm), corresponding to (100) and (101) planes of  $WS_2$  respectively, (d) HRTEM of the edge of the flake corresponding to the circled area shown in figure (c) with highlighted the 7 nm thick edge corresponding to 11 layers. The inset shows the Selected Area Electron Diffraction (SAED) of the flake.

To give a statistical insight of the reproducibility of the preparation, four different suspensions were prepared after 2 h milling and 90 min sonication and the corresponding centrifuged suspensions collected, and spin coated on  $Si_3N_4$  substrates (see experimental section). Figure 4a–d shows the AFM images of each prepared sample covering an area of  $10 \times 10 \mu m^2$  and corresponding to a total population of  $\approx 220$  flakes. Overall, flakes' thickness follows a log-normal distribution as shown in Figure 4e, indicating that almost 30% of the flakes are  $\leq 3.0$  nm thick (i.e.,  $\approx 5$  layers) and that about

75% are  $\leq 6$  nm (i.e.,  $\approx 10$  layers). Moreover, as displayed in Figure 4f, average flake lateral dimensions are approximately  $\approx 110$  nm, yielding a surface coverage of  $\approx 6\%$ , as shown in Figure 4g. The overall calculated “aspect ratio” is 27.5, which is comparable to the ones previously reported for MoS<sub>2</sub> and WS<sub>2</sub>, given the same preparation methodology [27,32]. The reduced standard deviations shown in Figure 4f,g attest to the high reproducibility of the exfoliation process.

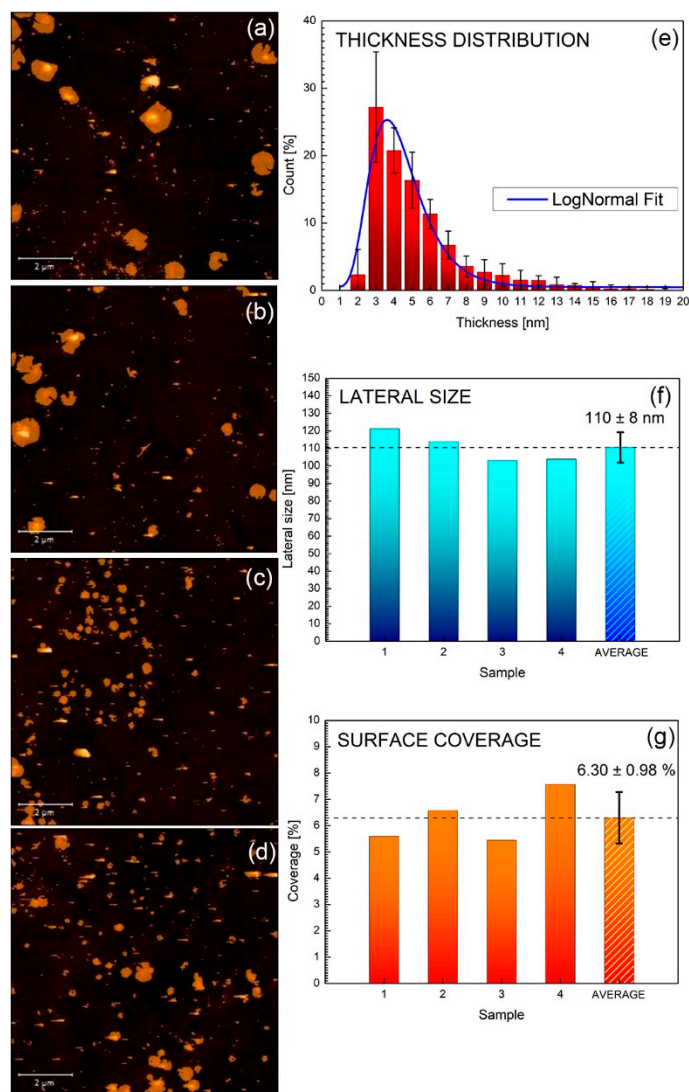


**Figure 4.** (a–d) AFM images of WS<sub>2</sub> exfoliated corresponding to four different samples prepared under the same conditions (i.e., 2 h ball milling and 90 min sonication). Statistical analysis corresponding to thickness distribution (e), Lateral dimensions (f) and surface area coverage (g).

### 3.2. Chemical Composition of the Exfoliated WS<sub>2</sub>

Chemical issues related to both the evolution of point defects and oxidation phenomena of TMDs highlight important challenges associated with the practical utilization of TMDs monolayers in electronic and optoelectronic devices. Sulphur vacancy is one of the most typical point defects in 2D MoS<sub>2</sub> and WS<sub>2</sub> monolayers [33], eventually leading to active sites for gas adsorption. On the other hand, spontaneous oxidation of metal sulphides into their metal oxide counterparts [34], may result in poor reproducibility of the gas-sensing response over the long-term, as discussed in our previous publication [26].

Figure 5, panel (a), reports the W 4f core level XPS spectra of the pristine commercial WS<sub>2</sub> powder (PWD). The two doublets corresponding to 4f<sub>7/2</sub> peaks are assigned, according to the literature, to WS<sub>2</sub>

and  $\text{WO}_3$ , respectively [35,36]. It turns out that the pristine powder is already oxidized, with a  $\text{WO}_3$  content of  $\approx 18\%$ . This phenomenon, is not surprising considering that spontaneous oxidation of  $\text{MoS}_2$  at room temperature after 6–12 months has been already reported in the literature, demonstrating the occurrence of ageing phenomena of  $\text{MoS}_2$  [25] and  $\text{WS}_2$  monolayers in ambient air [26]. Figure 5b shows that after exfoliation, the  $\text{WO}_3$  content decreases to  $\approx 16\%$ . This could be explained considering that by grinding and sonicating  $\text{WS}_2$  powders, newly not-yet-oxidized surfaces are formed, resulting in a smaller content of  $\text{WO}_3$ , as evidenced by XPS measurements. Furthermore, as discussed in the next paragraph, given the optimum operating temperature for gas sensing at  $150\text{ }^\circ\text{C}$ , exfoliated  $\text{WS}_2$  suspensions, were therefore drop-casted and pre-annealed at  $180\text{ }^\circ\text{C}$  for 1 h in air to stabilize the oxidation levels. As shown in Figure 5c, after annealing, the  $\text{WO}_3$  content increased to  $\approx 58\%$ .

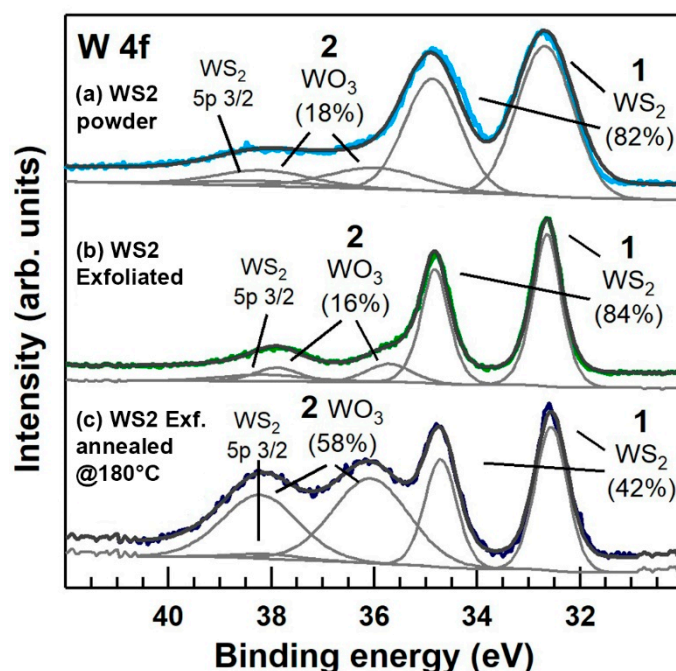


**Figure 5.** X-Ray Photoemission Spectroscopy (XPS) spectra of W 4f core level acquired respectively on (a) pristine  $\text{WS}_2$  commercial powder ( $\text{WS}_2$  PWD), (b) Exfoliated  $\text{WS}_2$  by ball milling and sonication at  $25\text{ }^\circ\text{C}$ , (c)  $\text{WS}_2$  exfoliated and post-annealed at  $180\text{ }^\circ\text{C}$ . All the components and their relative atomic percentages are labelled in the figure.

Regarding sulphur vacancies formation, considering 1% the detection limit of the XPS measurement, we found no clear evidence of defects of sulfur vacancies-related components (typically at binding energies of  $\approx 36.1$  in the W 4f core level XPS spectra in Figure 5). The analysis of the S 2p core level XPS spectra, reported in Supplementary Figure S3, is in line with the analysis reported for the W 4f.

Figure 6 displays the Raman spectra of bulk powder, exfoliated flakes and  $180\text{ }^\circ\text{C}$  annealed film. Peaks located at  $350$  and  $419\text{ cm}^{-1}$  refer to crystalline  $\text{WS}_2$ . The peak at  $520\text{ cm}^{-1}$  corresponds to the substrate (i.e., crystalline  $\text{SiO}_2$ ). Raman spectra reveal that neither crystalline nor amorphous  $\text{WO}_3$  are formed. According to the literature [37], the displacement of crystalline  $\text{WO}_3$  is excluded considering that no peaks corresponding to the dashed lines at  $719$  and  $807\text{ cm}^{-1}$  are observed. No signals of amorphous  $\text{WO}_3$  were shown, as attested by the absence of a broad peak between  $600$  and  $900\text{ cm}^{-1}$ , attributed to the W-O stretching vibration of amorphous  $\text{WO}_3$ . The lack from the Raman spectra of any  $\text{WO}_3$  signal, as opposed to XPS, can be explained considering that Raman spectroscopy penetrates more deeply inside the material, suggesting that the overall amount of  $\text{WO}_3$  throughout the whole flakes is negligible.

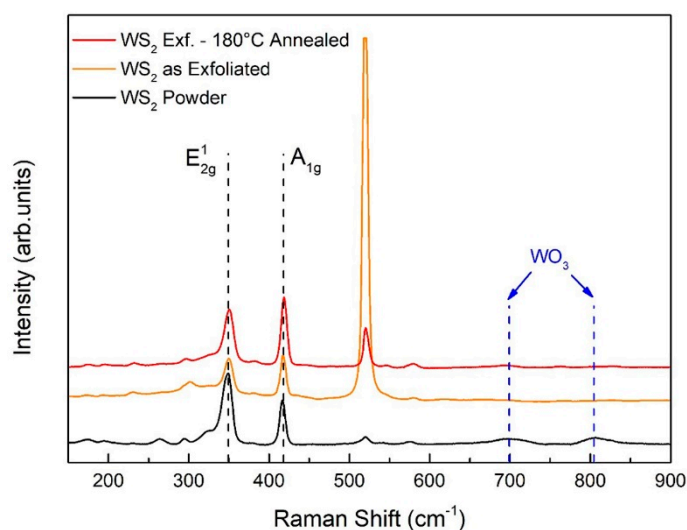


**Figure 6.** Raman spectra of WS<sub>2</sub> bulk powder, WS<sub>2</sub> as-exfoliated and WS<sub>2</sub> flakes post-annealed at 180 °C.

In order to have a better understanding where the as-formed WO<sub>3</sub> is located, firstly we have to consider that both XPS and Raman techniques give information on the chemical bonding of the elements, secondly that XPS information comes from photoelectrons escaping maximum up to 10 nm below the material surface, lastly that Raman spectroscopy, compared to XPS, is a “bulk” technique (given the negligible attenuation of visible light at the length scale of microns). It turns out that the WS<sub>2</sub>/WO<sub>3</sub> percentage content measured by XPS and shown in Figure 4 (i.e., ≈ 58%), represents the average chemical compositions of a portion of the material confined within at last 10 nm from the material surface. This region, for simplicity, can be referred as a “surface layer”, which represents the reacting surface to interfering gases. Regarding the crystallographic nature of the “surface layer”, grazing incidence XRD diffraction carried on exfoliated and 200 °C annealed WS<sub>2</sub> flakes (shown in Supplementary Figure S4) revealed the occurrence of peaks belonging only to WS<sub>2</sub>, thus excluding the formation of any crystalline WO<sub>3</sub> in the 180 °C annealed film. It may be concluded that the “surface layer” is a composite structure comprising amorphous WO<sub>3</sub> and pristine crystalline WS<sub>2</sub>. These experimental results are in line with that previously discussed in the literature [38], that the oxidation of bulk TMDs provides two parallel steps. Oxygen atoms rapidly exchange with surface sulphur forming an amorphous oxide layer, whilst WS<sub>2</sub> interlayer channels provide a path for inward-oxygen and backward-sulphur diffusion, resulting in the formation of amorphous WO<sub>3</sub>, which propagates over time inside the TMD flakes.

### 3.3. Gas Sensing Response

It has been reported that TMDs gas sensors operating at room temperature have shown remarkable limitations, largely related to irreversible desorption of the gas molecules, displaying incomplete recovery of the baseline at 25 °C [39,40]. The selection of the best operating temperature (OT), which it corresponds the complete base line recovery, within reasonable response times, and acceptable gas relative responses (RR), is limited in TMDs by the intensifying of the oxidation processes with increasing the OT, as previously discussed. Baseline recovery and response times depend on the adsorption-desorption kinetic of gases with the sensor surface, which eventually improves with increasing the OT. RR is mostly related to microstructure (i.e., surface area, grain size), concentration of surface defects (i.e., oxygen or sulphur vacancies) and structure of the reacting surface (crystalline or amorphous). To find the best OT exfoliated WS<sub>2</sub> drop casted on Si<sub>3</sub>N<sub>4</sub> substrates were previously air annealed at 180 °C to stabilize the WO<sub>3</sub> content up to ≈ 58%, as shown in Figure 5c. Afterwards,



different OT in the 50–150 °C temperature range where tested, resulting in 150 °C as the best OT, as shown in Supplementary Figure S5.

The Scanning Electron Microscopy (SEM) picture of the sensing device shown in Figure 7 highlights a homogeneous distribution of annealed flakes, enabling current percolation paths between adjacent flakes, covering an area of  $1.4 \times 0.6 \text{ mm}^2$  over 30  $\mu\text{m}$  spaced Pt interdigitated electrodes.

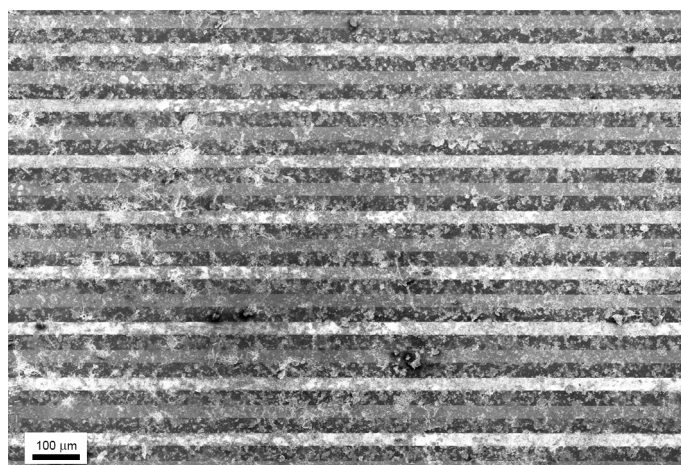


**Figure 7.** SEM image of sensor obtained by drop casting exfoliated  $\text{WS}_2$  and annealing at 180 °C on  $\text{Si}_3\text{N}_4$  substrate provided with Pt finger-type electrodes (30 microns apart).

Figure 8a shows the normalized dynamic resistance changes, at 150 °C OT of few-layers  $\text{WS}_2$  thin films to  $\text{NO}_2$  and  $\text{H}_2$  in the 100 ppb–5 ppm and 1 ppm–250 ppm gas concentration ranges, respectively.  $\text{WS}_2$  films respond as  $n$ -type semiconductors with decreasing/increasing resistance upon exposure to  $\text{H}_2/\text{NO}_2$ , respectively. Degassing with dry air at 150 °C OT, the baseline resistance (BLR), as indicated by the black dotted line in the figure, is almost recovered.  $\text{WS}_2$  flakes are more sensitive to  $\text{NO}_2$  than  $\text{H}_2$  gas, with associated low detection limits (LDL) of 200 ppb and 5 ppm respectively, confirming what has been previously reported in the literature.

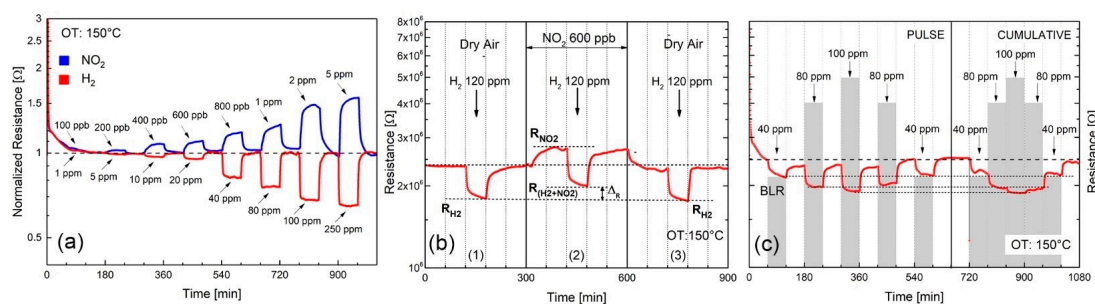


**Figure 8.** Electrical responses of the exfoliated  $\text{WS}_2$  post-annealed at 180 °C, at 150 °C operating temperature in dry air. (a) Comparison of the normalized dynamic response to  $\text{NO}_2$  (100 ppb–5 ppm) and  $\text{H}_2$  (1–250 ppm), (b)  $\text{NO}_2$  cross-sensitivity to  $\text{H}_2$ : first panel, the response to 120 ppm  $\text{H}_2$  in dry air, second panel, response to 120 ppm  $\text{H}_2$  with 600 ppb  $\text{NO}_2$ , third panel, response to 120 ppm  $\text{H}_2$  (as to first panel) for comparison, (c) Reproducibility and baseline recovery by exposing the film to both pulse and cumulative  $\text{H}_2$  concentrations in the range 40–100 ppm.  $\text{H}_2$  concentrations are highlighted in the figure by grey shadowed rectangular plots.

Cross-sensitivity, which represent the ability of  $\text{WS}_2$  to detect  $\text{H}_2$  in the presence of  $\text{NO}_2$  interfering gas, has been shown in Figure 8b. Panel (1) of Figure 8b shows the  $\text{WS}_2$  response to  $\text{H}_2$  alone in dry air carrier at 150 °C OT. The “cross-sensitivity” produced by interfering  $\text{NO}_2$  to the measure of  $\text{H}_2$  is displayed in panel (2) of Figure 8b. By exposing to 600 ppb  $\text{NO}_2$ , sensor resistance initially increases,

yielding at equilibrium the resistance value  $R_{\text{NO}_2}$ . As soon as 120 ppm  $\text{H}_2$  is introduced, the resistance decreases, yielding the equilibrium value shown as  $R_{(\text{H}_2+\text{NO}_2)}$ . The cross-sensitivity effect is displayed in the picture as  $(\Delta R)$ , to indicate the gap between the electrical resistance to 120 ppm  $\text{H}_2$  alone (i.e.,  $R_{\text{H}_2}$ ) and that in the presence of 120 ppm  $\text{H}_2$  and 600 ppb  $\text{NO}_2$  (i.e.,  $R_{(\text{H}_2+\text{NO}_2)}$ ). These results imply that the response to 120 ppm  $\text{H}_2$  is affected by the presence of a small amount (i.e., 600 ppb), of  $\text{NO}_2$  interfering gas, confirming the stronger affinity of  $\text{WS}_2$  to detect  $\text{NO}_2$  as respect to  $\text{H}_2$ .

Reproducibility of the electrical response to pulse (on/off) and cumulative modes  $\text{H}_2$  gas adsorption is shown in Figure 8c, demonstrating acceptable response characteristics to  $\text{H}_2$ . Under pulsed conditions, the baseline resistance (BLR) fully regains its initial value after completion of each desorption cycle in dry air. Under cumulative stepwise adsorption/desorption mode, the  $\text{H}_2$  gas resistance increases/decreases steadily, matching almost the same  $\text{H}_2$  resistance values obtained under pulsed conditions (black lines at saturation correspond to 40, 80 and 100 ppm  $\text{H}_2$ ).

Selectivity tests to both oxidizing and reducing gases carried out at 150 °C operating temperature with respect to 5 ppm  $\text{NO}_2$ , exhibit satisfactory  $\text{WS}_2$  selectivity to both 5 ppm  $\text{H}_2$  and  $\text{NH}_3$  gases and to 250 ppm ethanol and acetone, as shown in Supplementary Figure S6. These data were demonstrated to be in line with previous research on  $\text{WS}_2$  nanoflakes synthesized by electrospinning [41].

Long-term stability properties of the electrical response of both baseline and saturation resistances to 800 ppb  $\text{NO}_2$  over a period of 12 months (corresponding to approximately 5 months of cumulative operations at 150 °C operating temperature) were also recorded. Figure 9a shows baseline resistances (lower curve) and saturation resistances corresponding to 800 ppb  $\text{NO}_2$  (upper curve), randomly collected over a period of 52 weeks. Average resistances with associated standard deviations are calculated over a set of 5 consecutive measurements. Relative responses (RR) taken over the investigated period are also highlighted in the figure. No remarkable fluctuations of both baseline and resistances at saturation were detectable, attesting good long-term stability of the electrical properties of the  $\text{WS}_2$  films. To validate the electrical responses shown in Figure 8a, we also investigated the oxidation state of the sensor surface, measuring the  $\text{WO}_3$  content before and after 52 weeks conditioning. Figure 9b compares the XPS W 4f signal of the as-exfoliated  $\text{WS}_2$  180 °C annealed film before (lower curve) and after 52 weeks long-term conditioning to different gases and 150 °C OT (upper curve). Beside an increase of the signal noise after long-term conditionings, no substantial increase of the  $\text{WO}_3$  content was detected. These observations imply that exfoliated  $\text{WS}_2$  films, previously stabilized at 180 °C, can satisfactorily respond to different gases under sustained conditions at 150 °C operating temperature.

Finally, the influence of humidity on  $\text{NO}_2$  and  $\text{H}_2$  gas response at 150 °C OT is also reported. Figure 10 shows the dynamic response of the films exposed to air with increasing amounts of humidity, in the 10–80% relative humidity (RH) range. The inset of Figure 10a displays the related sensitivity plot. Considering that at 150 °C operating temperature physisorbed water is reasonably evaporated, it is unlikely that the decrease of the resistance is induced by a protonic surface charge-transfer mechanism, as reported for  $\text{WS}_2$  humidity sensors operating at room temperature [42]. More reasonably, water vapor at 150 °C OT behaves like a reducing gas inducing a steady resistance decrease in  $\text{WS}_2$  *n*-type semiconductor, which does not saturate with increasing the RH, as shown in the inset of Figure 10a.

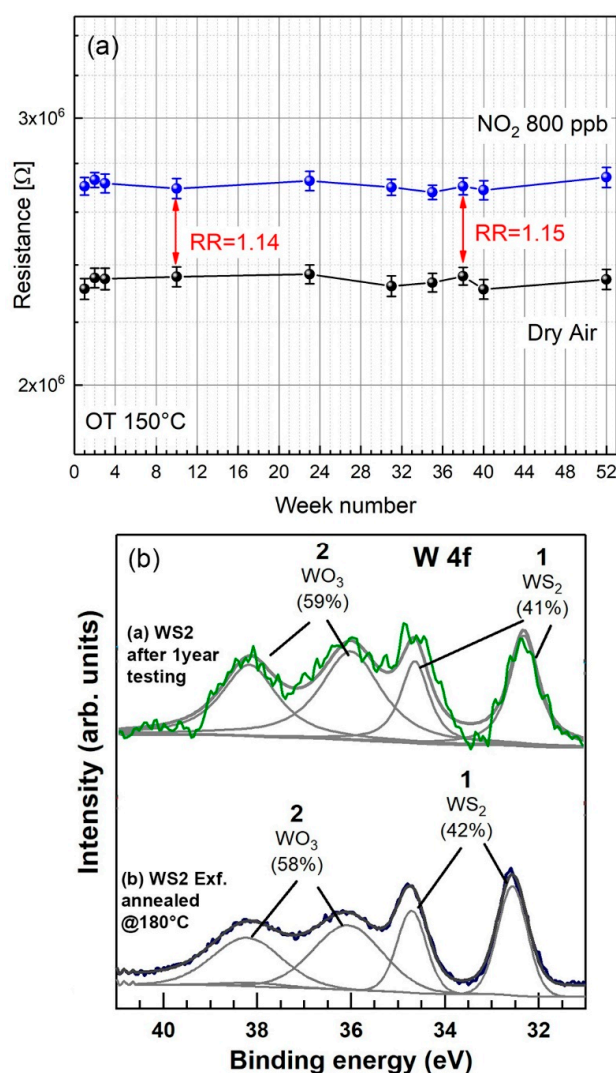


**Figure 9.** WS<sub>2</sub> exfoliated and post-annealed at 180 °C. (a) Long-term stability properties of the electrical resistances of the baseline (lower curve) and 800 ppb NO<sub>2</sub> over a period of 12 months (equivalent to approximately 5 months of continuous operation at 150 °C operating temperature). Average resistance values with associated standard deviations are calculated over a set of 5 consecutive measurements. (b) Comparison of the XPS signals of the as-exfoliated WS<sub>2</sub> annealed at 180 °C (lower curve) and the same sample after one-year conditioning to various gases and 150 °C operating temperature.

In order to evaluate the influence of humidity to NO<sub>2</sub> and H<sub>2</sub> gases response, cross-sensitivity tests have been performed. Figure 10b, c shows the dynamic responses to different NO<sub>2</sub> and H<sub>2</sub> concentrations, measured in humid air at 40% RH. As soon as water vapor is introduced, a downshift of the baseline from BLR<sub>DRY</sub> to BLR<sub>H<sub>2</sub>O</sub> is shown. NO<sub>2</sub> and H<sub>2</sub> dynamic responses in dry and 40% RH are almost similar, as shown in Figures 8a and 10b,c. Comparison of the NO<sub>2</sub> and H<sub>2</sub> gases sensitivities in dry and 40% RH air are shown in Figure 10d. Notably, no significant differences are displayed as respect to slopes of the calibrating curves (i.e., sensitivity) and relative responses values (i.e., Ra/Rg), attesting that both NO<sub>2</sub> and H<sub>2</sub> measurements are not affected by the presence of moisture.

These results, indeed, demonstrate the possibility to produce efficient and reproducible gas sensors, able to detect NO<sub>2</sub> and H<sub>2</sub> with no significant cross-sensitivity effects induced by humid air in the 10–80% RH range and 150 °C operating temperature.

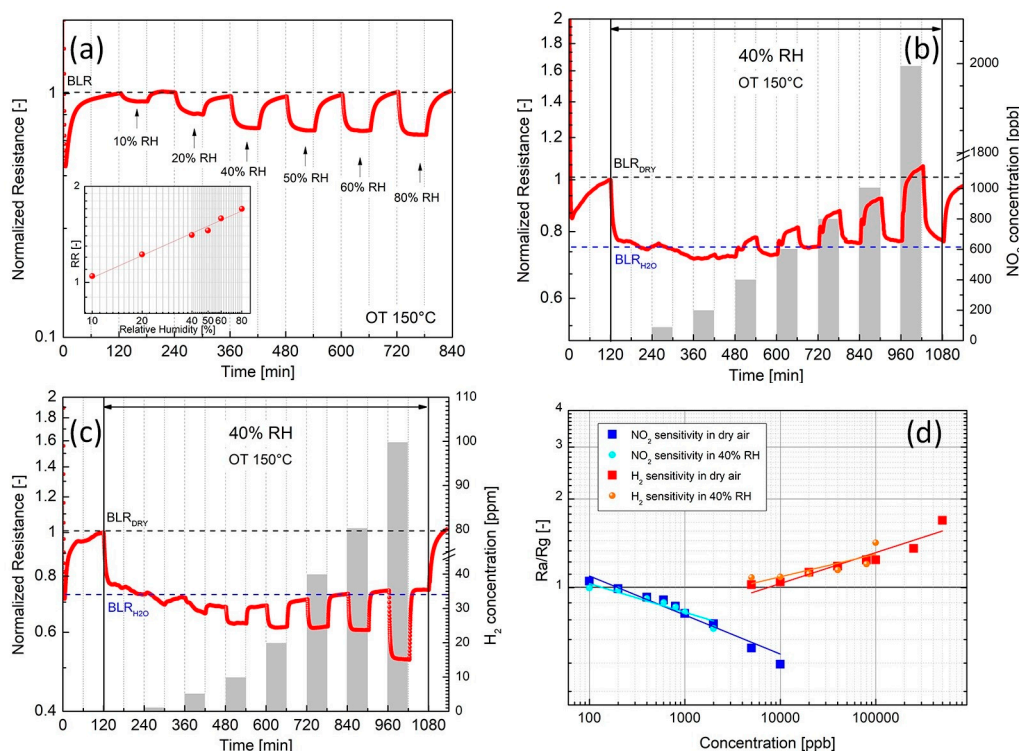


**Figure 10.** Electrical responses of the exfoliated WS<sub>2</sub> post-annealed at 180 °C (150 °C operating temperature) to different Relative Humidity (RH) conditions. (a) Normalized dynamic response to humidity (10–80% RH). The inset depicts the corresponding sensitivity plot. (b) Dynamic response to increasing NO<sub>2</sub> concentrations in air with 40% RH, (c) Dynamic response to increasing H<sub>2</sub> concentrations in air with 40% RH, (d) Comparison of the sensitivity plots to NO<sub>2</sub> and H<sub>2</sub> in dry air and 40% RH, respectively.

### 3.4. Gas Response Mechanism

As previously discussed, by annealing the exfoliated WS<sub>2</sub> at 180 °C a “surface layer” containing ≈58% of amorphous WO<sub>3</sub>, penetrating at least 10 nm from the surface, is formed. It turns out that both structure and chemical composition of the “Surface layer”, comprising crystalline WS<sub>2</sub> and amorphous WO<sub>3</sub>, strongly influence the gas response mechanism.

HRTEM investigations of the pre-annealed 180 °C sample shown in Figure 11, display the occurrence of a complex surface patchwork comprising amorphous WO<sub>3</sub> regions (located inside the green square of Figure 11b), possibly rearranging as not-connected, amorphous, isolated-clusters which are eventually embedded in crystalline WS<sub>2</sub> phase (located inside the red square of Figure 11b).

To investigate the contribution of single WO<sub>3</sub> on to the electrical properties of WS<sub>2</sub>/WO<sub>3</sub> pre-annealed composite, we have prepared a fully-oxidized WS<sub>2</sub>, containing ≈ 99% amorphous WO<sub>3</sub> and tested to NO<sub>2</sub>. This sample has been prepared by the same exfoliation method by grinding and drying WS<sub>2</sub> powders at 25 °C, but setting the sonicating temperature at 60 °C, instead of 25 °C for 90 min, and finally pre-annealing in dry air at 180 °C.

Figure 12a,b shows the XPS and grazing incidence XRD patterns of the fully oxidized film, attesting that the chemical composition of the “surface layer” is ≈ 99% WO<sub>3</sub> (Figure 12a) and that the as-formed WO<sub>3</sub> is amorphous, as highlighted by the absence of WO<sub>3</sub> peaks inside the inset of the XRD pattern of Figure 12b. It turns out that the fully oxidized region possibly covers the whole surface of the flakes, not extending to the core, which maintain the crystalline structure of pristine exfoliated WS<sub>2</sub> (as attested by the presence of WS<sub>2</sub> peaks in the XRD pattern of Figure 12b). The electrical response of the fully oxidized amorphous WO<sub>3</sub> to 800 ppb NO<sub>2</sub> and different operating temperatures in dry air is

shown in Figure 12c. According to Figure 12c, amorphous  $\text{WO}_3$  is not responsive to  $\text{NO}_2$  gas in dry air, in the operating temperature range 75–150 °C.

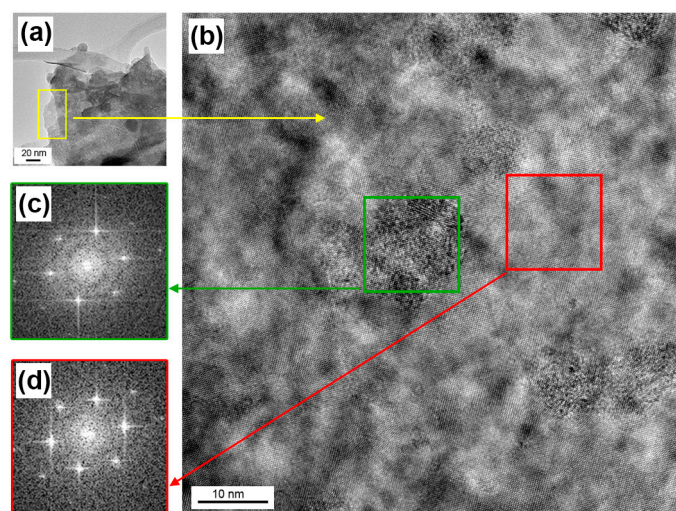


**Figure 11.** HRTEM images of the  $\text{WS}_2$  film pre-annealed at 180 °C. (b) Magnification of the yellow area of Figure 11 (a) displaying the presence of ordered structures (i.e., inside the red square) referred to crystalline  $\text{WS}_2$  and the presence of disordered ones (i.e., inside the green square) attributed to amorphous  $\text{WO}_3$ . Related Selected Area Electron Diffraction (SAED) patterns are shown in (c) and (d), highlighting the occurrence of sharper reflections (d) associated to crystalline  $\text{WS}_2$ .

Literature reports discussing the gas sensing properties of amorphous  $\text{WO}_3$  are very scarce. Some authors found no gas response to  $\text{NO}_x$  of amorphous  $\text{WO}_3$  deposited by sputtering [43] whereas others demonstrated negligible  $\text{NO}_2$  response using photochemically-produced amorphous  $\text{WO}_3$  [44]. In most cases, the  $\text{NO}_2$  gas response of amorphous  $\text{WO}_3$  is smaller with respect to crystalline  $\text{WO}_3$ , frequently associated with baseline drift phenomena, with few exceptions, mostly related to the preparation conditions. In our case, we demonstrated that the interaction of  $\text{NO}_2$  with amorphous 99%  $\text{WO}_3$  has no effects altogether.

Having shown in Figure 8a the substantial  $\text{NO}_2$  and  $\text{H}_2$  gas response of the  $\text{WO}_3/\text{WS}_2$  composite, we conclude that it is crystalline  $\text{WS}_2$  which primarily respond to  $\text{NO}_2$  gas. The predominant gas sensing role played by crystalline  $\text{WS}_2$  with respect to amorphous  $\text{WO}_3$ , is also supported by the decrease of the electrical resistance with increasing relative Humidity (RH), as shown in Figure 10a. Considering that  $\text{WO}_3$  interacts with humidity by increasing the resistance, due to  $\text{WO}_3$  lattice oxidation induced by humidity, as reported in the literature [45], the resistance decrease displayed in Figure 10a rules out any significant contribution of  $\text{WO}_3$  to the overall humidity response. Moreover, the hypothesis that  $\text{WS}_2$  is likely to be the responding material is also supported by our previous research, which demonstrated that humidity decreases the sensor resistance in  $\text{MoS}_2$ -based exfoliated [25].

Discussing the contribution of crystalline  $\text{WS}_2$  to the overall electrical resistance, it was recently demonstrated by first-principles calculations on single  $\text{MoS}_2$  sulphur-defective layer that  $\text{O}_2$  irreversibly chemisorbs on sulphur vacancies [46] and that the “heal” of these defects by substitutional O atoms is thermodynamically favorable [47]. Furthermore, in case of direct  $\text{NO}_2$  molecules interaction with sulphur vacancies, a dissociative adsorption of  $\text{NO}_2$ , leading to O atoms passivating the vacancies, and NO molecules physisorbed on the  $\text{MoS}_2$  surface, was also proposed [48,49]. Given these premises, we hypothesize that both  $\text{O}_2$  and  $\text{NO}_2$  suppress sulphur vacancies, supporting a gas response mechanism based only on physisorption of  $\text{NO}_2$  and  $\text{H}_2$  molecules on passivated (i.e., defect-free)  $\text{WS}_2$  surface. This hypothesis is sustained by theoretical studies on the adsorption of  $\text{NO}_2$ ,  $\text{H}_2$ ,  $\text{O}_2$ ,  $\text{H}_2\text{O}$ ,  $\text{NH}_3$  and CO gases on defect-free single layer  $\text{MoS}_2$  and  $\text{WS}_2$  [50,51]. According to this physisorption model, the size and sign of the resistance changes, when exposing few-flakes of  $\text{WS}_2$  to oxidizing ( $\text{NO}_2$ ) and

reducing ( $H_2$ ) gases, depend on the number of exchanged carriers (i.e., electrons) and their direction.  $NO_2$  being more electronegative than  $H_2$  induces a large electron withdrawal, whereas  $H_2$  results in weak electron injection, explaining the increase/decrease of electrical resistance in  $n$ -type  $WS_2$ , as well as the smaller detection limit measured for  $NO_2$  (200 ppb) as compared to the one found for  $H_2$  (i.e., 5 ppm).

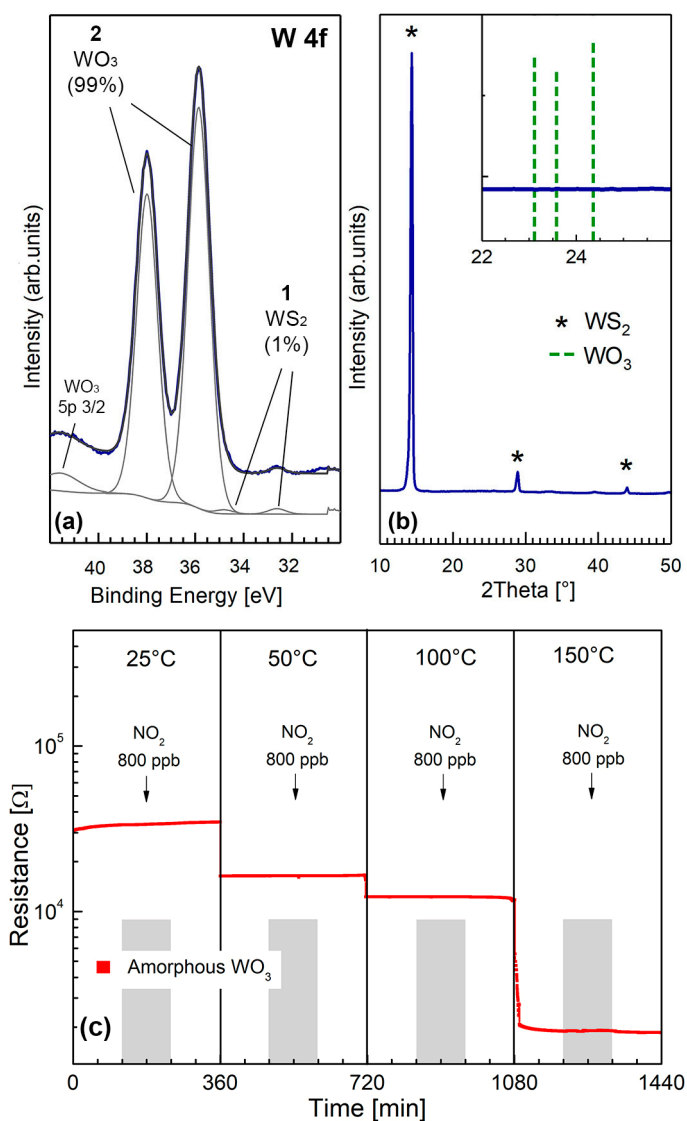


**Figure 12.** Chemical composition, crystalline structure and microstructural features of a fully oxidized  $WO_3$  thin film. (a) W 4f core level XPS spectra, (b) XRD grazing incidence spectra. Top right inset shows the close up of the  $2\theta$  region characteristic of crystalline  $WO_3$  (corresponding peaks of crystalline  $WO_3$ , according to ICDS 98-001-7003, are highlighted by dashed green lines), (c) electrical response of the fully oxidized  $WO_3$  amorphous film to  $NO_2$  and different OTs.

Lastly, a question to be resolved is why both  $NO_2$  and  $H_2$  sensitivities are not affected by the presence of moisture, as shown in Figure 10d. This behavior may suggest that water vapor adsorbs on to the  $WS_2$  surface with a different and non-competitive mechanism with respect to  $NO_2$  and  $H_2$  gases. Clearly this interaction is a complex issue, and is yet to be clarified based on specific theoretical and experimental studies.

#### 4. Conclusions

In conclusion, we have demonstrated an effective, reproducible and high-yield exfoliation process, obtained by enhanced low energy ball milling and sonication. Specifically, the two-step exfoliation followed by drop casting the centrifuged suspension leads to the deposition of thin films of well-packed and interconnected WS<sub>2</sub> flakes with controlled and reproducible microstructure over large areas, thus representing a fast, simple and scalable method, compatible with standard microelectronic fabrication techniques. We found that a spontaneous oxidation of WS<sub>2</sub> leading to the formation of amorphous WO<sub>3</sub> on the surface of the exfoliated WS<sub>2</sub> takes place, addressing the crucial drawback of surface oxidation of TMDs. We also found that by pre-annealing the WS<sub>2</sub> films at 180 °C, a reproducible surface oxidation of WS<sub>2</sub> to amorphous WO<sub>3</sub> takes place, which stabilize from further oxidation the WS<sub>2</sub> layers. Reproducible gas sensing responses to NO<sub>2</sub> and H<sub>2</sub> and humidity at 150 °C operating temperature were achieved with detection limits of 200 ppb and 5 ppm to NO<sub>2</sub> and H<sub>2</sub>, respectively. The cross-sensitivity test highlighted a weak interference played by NO<sub>2</sub> to the H<sub>2</sub> gas response. Water vapor at 40% RH also resulted in having no interference to the measure of NO<sub>2</sub> and H<sub>2</sub> gases, attesting promising characteristics of WS<sub>2</sub> exfoliated films for gas sensing applications.

**Supplementary Materials:** The following are available online at <http://www.mdpi.com/2079-4991/9/10/1363/s1>, Figure S1: Schematic illustration of the exfoliation process, Figure S2: Schematic illustration of the gas sensing equipment, Figure S3: XPS spectra of S 2p core level, Figure S4: Grazing incidence XRD spectra of the as-exfoliated WS<sub>2</sub>; as-exfoliated WS<sub>2</sub>—200 °C annealed for 1 h, Figure S5: The electrical response of WS<sub>2</sub> post-annealed at 180 °C at different operating temperatures and 800 ppb NO<sub>2</sub> in dry air, Figure S6: Selectivity response of WS<sub>2</sub> post-annealed at 180 °C at 150 °C operating temperature.

**Author Contributions:** Conceptualization, L.O., C.C., V.P. and S.M.E.; methodology, L.O. and C.C.; validation, L.O. and C.C.; formal analysis, V.P.; investigation, V.P. and S.M.E.; resources, C.C., L.O. and M.N.; data curation, V.P. and S.M.E.; supervision, L.O. and C.C.; writing—original draft preparation, V.P., S.M.E. and C.C.; writing—review and editing, C.C., L.O. and V.P.

**Funding:** This research was funded by REGIONE ABRUZZO Dipartimento Sviluppo Economico, Politiche del Lavoro, Istruzione, Ricerca e Università Servizio Ricerca e Innovazione Industriale for financial support through progetto POR FESR Abruzzo 2018–2020 Azione 1.1.1 e 1.1.4—“Studio di soluzioni innovative di prodotto e di processo basate sull’utilizzo industriale dei materiali avanzati” CUP n. C17H18000100007.

**Conflicts of Interest:** The authors declare no conflict of interest. The funders had no role in the design of the study, in the collection, analyses, or interpretation of data, in the writing of the manuscript, or in the decision to publish the results.

#### References

1. Yang, W.; Gan, L.; Li, H.; Zhai, T. Two-dimensional layered nanomaterials for gas-sensing applications. *Inorg. Chem. Front.* **2016**, *3*, 433–451. [[CrossRef](#)]
2. Late, D.J.; Huang, Y.K.; Liu, B.; Acharya, J.; Shirodkar, S.N.; Luo, J.; Yan, A.; Charles, D.; Waghmare, U.V.; Dravid, V.P.; et al. Sensing behavior of atomically thin-layered MoS<sub>2</sub> transistors. *ACS Nano* **2013**, *7*, 4879–4891. [[CrossRef](#)] [[PubMed](#)]
3. Voiry, D.; Yamaguchi, H.; Li, J.; Silva, R.; Alves, D.C.B.; Fujita, T.; Chen, M.; Asefa, T.; Shenoy, V.B.; Eda, G.; et al. Enhanced catalytic activity in strained chemically exfoliated WS<sub>2</sub> nanosheets for hydrogen evolution. *Nat. Mater.* **2013**, *12*, 850–855. [[CrossRef](#)] [[PubMed](#)]
4. Voiry, D.; Yang, J.; Chhowalla, M. Recent Strategies for Improving the Catalytic Activity of 2D TMD Nanosheets Toward the Hydrogen Evolution Reaction. *Adv. Mater.* **2016**, *28*, 6197–6206. [[CrossRef](#)] [[PubMed](#)]
5. Mak, K.F.; Shan, J. Photonics and optoelectronics of 2D semiconductor transition metal dichalcogenides. *Nat. Photonics* **2016**, *10*, 216–226. [[CrossRef](#)]
6. Shim, J.; Park, H.-Y.; Kang, D.-H.; Kim, J.-O.; Jo, S.-H.; Park, Y.; Park, J.-H. Electronic and Optoelectronic Devices based on Two-Dimensional Materials: From Fabrication to Application. *Adv. Electron. Mater.* **2017**, *3*, 1600364. [[CrossRef](#)]
7. Pumera, M.; Sofer, Z.; Ambrosi, A. Layered transition metal dichalcogenides for electrochemical energy generation and storage. *J. Mater. Chem. A* **2014**, *2*, 8981–8987. [[CrossRef](#)]
8. Wang, H.; Feng, H.; Li, J. Graphene and graphene-like layered transition metal dichalcogenides in energy conversion and storage. *Small* **2014**, *10*, 2165–2181. [[CrossRef](#)]

9. Gupta, A.; Sakthivel, T.; Seal, S. Recent development in 2D materials beyond graphene. *Prog. Mater. Sci.* **2015**, *73*, 44–126. [[CrossRef](#)]
10. Bhimanapati, G.R.; Lin, Z.; Meunier, V.; Jung, Y.; Cha, J.; Das, S.; Xiao, D.; Son, Y.; Strano, M.S.; Cooper, V.R.; et al. Recent Advances in Two-Dimensional Materials beyond Graphene. *ACS Nano* **2015**, *9*, 11509–11539. [[CrossRef](#)]
11. Yang, D.; Frindt, R.F. Li-intercalation and exfoliation of WS<sub>2</sub>. *J. Phys. Chem. Solids* **1996**, *57*, 1113–1116. [[CrossRef](#)]
12. Ambrosi, A.; Sofer, Z.; Pumera, M. Lithium intercalation compound dramatically influences the electrochemical properties of exfoliated MoS<sub>2</sub>. *Small* **2015**, *11*, 605–612. [[CrossRef](#)] [[PubMed](#)]
13. Nicolosi, V.; Chhowalla, M.; Kanatzidis, M.G.; Strano, M.S.; Coleman, J.N. Liquid Exfoliation of Layered Materials. *Science* **2013**, *340*, 1226419. [[CrossRef](#)]
14. Niu, L.; Coleman, J.N.; Zhang, H.; Shin, H.; Chhowalla, M.; Zheng, Z. Production of Two-Dimensional Nanomaterials via Liquid-Based Direct Exfoliation. *Small* **2016**, *12*, 272–293. [[CrossRef](#)] [[PubMed](#)]
15. Yi, M.; Shen, Z. A review on mechanical exfoliation for the scalable production of graphene. *J. Mater. Chem. A* **2015**, *3*, 11700–11715. [[CrossRef](#)]
16. Kumar, G.R.; Jayasankar, K.; Das, S.K.; Dash, T.; Dash, A.; Jena, B.K.; Mishra, B.K. Shear-force-dominated dual-drive planetary ball milling for the scalable production of graphene and its electrocatalytic application with Pd nanostructures. *RSC Adv.* **2016**, *6*, 20067–20073. [[CrossRef](#)]
17. Abdelkader, A.M.; Kinloch, I.A. Mechanochemical Exfoliation of 2D Crystals in Deep Eutectic Solvents. *ACS Sustain. Chem. Eng.* **2016**, *4*, 4465–4472. [[CrossRef](#)]
18. Krishnamoorthy, K.; Pazhamalai, P.; Veerasubramani, G.K.; Kim, S.J. Mechanically delaminated few layered MoS<sub>2</sub> nanosheets based high performance wire type solid-state symmetric supercapacitors. *J. Power Sources* **2016**, *321*, 112–119. [[CrossRef](#)]
19. Yao, Y.; Tolentino, L.; Yang, Z.; Song, X.; Zhang, W.; Chen, Y.; Wong, C.P. High-concentration aqueous dispersions of MoS<sub>2</sub>. *Adv. Funct. Mater.* **2013**, *23*, 3577–3583. [[CrossRef](#)]
20. Perkins, F.K.; Friedman, A.L.; Cobas, E.; Campbell, P.M.; Jernigan, G.G.; Jonker, B.T. Chemical Vapor Sensing with Monolayer MoS<sub>2</sub>. *Nano Lett.* **2013**, *13*, 668–673. [[CrossRef](#)]
21. Liu, B.; Chen, L.; Liu, G.; Abbas, A.N.; Fathi, M.; Zhou, C. High-Performance Chemical Sensing Using Schottky-Contacted Chemical Vapor Deposition Grown Monolayer MoS<sub>2</sub> Transistors. *ACS Nano* **2014**, *8*, 5304–5314. [[CrossRef](#)] [[PubMed](#)]
22. Kuru, C.; Choi, D.; Kargar, A.; Liu, C.H.; Yavuz, S.; Choi, C.; Jin, S.; Bandaru, P.R. High-performance flexible hydrogen sensor made of WS<sub>2</sub> nanosheet–Pd nanoparticle composite film. *Nanotechnology* **2016**, *27*, 195501. [[CrossRef](#)] [[PubMed](#)]
23. Prezioso, S.; Perrozzi, F.; Giancaterini, L.; Cantalini, C.; Treossi, E.; Palermo, V.; Nardone, M.; Santucci, S.; Ottaviano, L. Graphene Oxide as a Practical Solution to High Sensitivity Gas Sensing. *J. Phys. Chem. C* **2013**, *117*, 10683–10690. [[CrossRef](#)]
24. Donarelli, M.; Ottaviano, L.; Giancaterini, L.; Fioravanti, G.; Perrozzi, F.; Cantalini, C. Exfoliated black phosphorus gas sensing properties at room temperature. *2D Mater.* **2016**, *3*, 025002. [[CrossRef](#)]
25. Donarelli, M.; Prezioso, S.; Perrozzi, F.; Bisti, F.; Nardone, M.; Giancaterini, L.; Cantalini, C.; Ottaviano, L. Response to NO<sub>2</sub> and other gases of resistive chemically exfoliated MoS<sub>2</sub>-based gas sensors. *Sens. Actuators B Chem.* **2015**, *207*, 602–613. [[CrossRef](#)]
26. Perrozzi, F.; Emamjomeh, S.M.M.; Paolucci, V.; Taglieri, G.; Ottaviano, L.; Cantalini, C. Thermal stability of WS<sub>2</sub> flakes and gas sensing properties of WS<sub>2</sub>/WO<sub>3</sub> composite to H<sub>2</sub>, NH<sub>3</sub> and NO<sub>2</sub>. *Sens. Actuators B Chem.* **2017**, *243*, 812–822. [[CrossRef](#)]
27. Nguyen, E.P.; Carey, B.J.; Daeneke, T.; Ou, J.Z.; Latham, K.; Zhuiykov, S.; Kalantar-zadeh, K. Investigation of two-solvent grinding-assisted liquid phase exfoliation of layered MoS<sub>2</sub>. *Chem. Mater.* **2015**, *27*, 53–59. [[CrossRef](#)]
28. Xing, T.; Mateti, S.; Li, L.H.; Ma, F.; Du, A.; Gogotsi, Y.; Chen, Y. Gas Protection of Two-Dimensional Nanomaterials from High-Energy Impacts. *Sci. Rep.* **2016**, *6*, 35532. [[CrossRef](#)]
29. Gutiérrez, H.R.; Perea-López, N.; Elías, A.L.; Berkdemir, A.; Wang, B.; Lv, R.; López-Urías, F.; Crespi, V.H.; Terrones, H.; Terrones, M.; et al. Extraordinary room-temperature photoluminescence in triangular WS<sub>2</sub> monolayers. *Nano Lett.* **2013**, *13*, 3447–3454. [[CrossRef](#)]
30. Ghorai, A.; Midya, A.; Maiti, R.; Ray, S.K. Exfoliation of WS<sub>2</sub> in the semiconducting phase using a group of lithium halides: A new method of Li intercalation. *Dalt. Trans.* **2016**, *45*, 14979–14987. [[CrossRef](#)]



31. Zhou, P.; Xu, Q.; Li, H.; Wang, Y.; Yan, B.; Zhou, Y.; Chen, J.; Zhang, J.; Wang, K. Fabrication of Two-Dimensional Lateral Heterostructures of WS<sub>2</sub>/WO<sub>3</sub>-H<sub>2</sub>O Through Selective Oxidation of Monolayer WS<sub>2</sub>. *Angew. Chem. Int. Ed.* **2015**, *54*, 15226–15230. [[CrossRef](#)] [[PubMed](#)]
32. Carey, B.J.; Daeneke, T.; Nguyen, E.P.; Wang, Y.; Zhen Ou, J.; Zhuiykov, S.; Kalantar-zadeh, K. Two solvent grinding sonication method for the synthesis of two-dimensional tungsten disulphide flakes. *Chem. Commun.* **2015**, *51*, 3770–3773. [[CrossRef](#)] [[PubMed](#)]
33. Hong, J.; Hu, Z.; Probert, M.; Li, K.; Lv, D.; Yang, X.; Gu, L.; Mao, N.; Feng, Q.; Xie, L.; et al. Exploring atomic defects in molybdenum disulphide monolayers. *Nat. Commun.* **2015**, *6*, 6293. [[CrossRef](#)] [[PubMed](#)]
34. Gao, J.; Li, B.; Tan, J.; Chow, P.; Lu, T.M.; Koratkar, N. Aging of Transition Metal Dichalcogenide Monolayers. *ACS Nano* **2016**, *10*, 2628–2635. [[CrossRef](#)] [[PubMed](#)]
35. Di Paola, A.; Palmisano, L.; Venezia, A.M.; Augugliaro, V. Coupled Semiconductor Systems for Photocatalysis. Preparation and Characterization of Polycrystalline Mixed WO<sub>3</sub>/WS<sub>2</sub> Powders. *J. Phys. Chem. B* **1999**, *103*, 8236–8244. [[CrossRef](#)]
36. Wong, K.C.; Lu, X.; Cotter, J.; Eadie, D.T.; Wong, P.C.; Mitchell, K.A.R. Surface and friction characterization of MoS<sub>2</sub> and WS<sub>2</sub> third body thin films under simulated wheel/rail rolling-sliding contact. *Wear* **2008**, *264*, 526–534. [[CrossRef](#)]
37. Shigesato, Y.; Murayama, A.; Kamimori, T.; Matsuhiro, K. Characterization of evaporated amorphous WO<sub>3</sub> films by Raman and FTIR spectroscopies. *Appl. Surf. Sci.* **1988**, *34*, 804–811. [[CrossRef](#)]
38. Margolin, A.; Rosentsveig, R.; Albu-Yaron, A.; Popovitz-Biro, R.; Tenne, R. Study of the growth mechanism of WS<sub>2</sub> nanotubes produced by a fluidized bed reactor. *J. Mater. Chem.* **2004**, *14*, 617–624. [[CrossRef](#)]
39. Long, H.; Harley-Trochimczyk, A.; Pham, T.; Tang, Z.; Shi, T.; Zettl, A.; Carraro, C.; Worsley, M.A.; Maboudian, R. High Surface Area MoS<sub>2</sub>/Graphene Hybrid Aerogel for Ultrasensitive NO<sub>2</sub> Detection. *Adv. Funct. Mater.* **2016**, *26*, 5158–5165. [[CrossRef](#)]
40. Long, H.; Chan, L.; Harley-Trochimczyk, A.; Luna, L.E.; Tang, Z.; Shi, T.; Zettl, A.; Carraro, C.; Worsley, M.A.; Maboudian, R. 3D MoS<sub>2</sub> Aerogel for Ultrasensitive NO<sub>2</sub> Detection and Its Tunable Sensing Behavior. *Adv. Mater. Interfaces* **2017**, *4*, 1700217. [[CrossRef](#)]
41. Wang, K.; Feng, W.L.; Qin, X.; Deng, D.S.; Feng, X.; Zhang, C. Tungsten sulfide nanoflakes: Synthesis by electrospinning and their gas sensing properties. *Zeitschrift für Naturforschung A J. Phys. Sci.* **2017**, *72*, 375–381. [[CrossRef](#)]
42. Jha, R.K.; Guha, P.K. Liquid exfoliated pristine WS<sub>2</sub> nanosheets for ultrasensitive and highly stable chemiresistive humidity sensors. *Nanotechnology* **2016**, *27*, 475503. [[CrossRef](#)] [[PubMed](#)]
43. Kim, T.S.; Kim, Y.B.; Yoo, K.S.; Sung, G.S.; Jung, H.J. Sensing characteristics of dc reactive sputtered WO<sub>3</sub> thin films as an NO<sub>x</sub> gas sensor. *Sens. Actuators B Chem.* **2000**, *62*, 102–108. [[CrossRef](#)]
44. Chu, C.W.; Deen, M.J.; Hill, R.H. Sensors for detecting sub-ppm NO<sub>2</sub> using photochemically produced amorphous tungsten oxide. *J. Electrochem. Soc.* **1998**, *145*, 4219–4225. [[CrossRef](#)]
45. Staerz, A.; Berthold, C.; Russ, T.; Wicker, S.; Weimar, U.; Barsan, N. The oxidizing effect of humidity on WO<sub>3</sub> based sensors. *Sens. Actuators B Chem.* **2016**, *237*, 54–58. [[CrossRef](#)]
46. Ma, D.; Wang, Q.; Li, T.; He, C.; Ma, B.; Tang, Y.; Lu, Z.; Yang, Z. Repairing sulfur vacancies in the MoS<sub>2</sub> monolayer by using CO, NO and NO<sub>2</sub> molecules. *J. Mater. Chem. C* **2016**, *4*, 7093–7101. [[CrossRef](#)]
47. Kc, S.; Longo, R.C.; Wallace, R.M.; Cho, K. Surface oxidation energetics and kinetics on MoS<sub>2</sub> monolayer. *J. Appl. Phys.* **2015**, *117*, 135301. [[CrossRef](#)]
48. Barsan, N.; Weimar, U. Conduction model of metal oxide gas sensors. *J. Electroceramics* **2001**, *7*, 143–167. [[CrossRef](#)]
49. Li, H.; Huang, M.; Cao, G. Markedly different adsorption behaviors of gas molecules on defective monolayer MoS<sub>2</sub>: A first-principles study. *Phys. Chem. Chem. Phys.* **2016**, *18*, 15110–15117. [[CrossRef](#)]
50. Yue, Q.; Shao, Z.; Chang, S.; Li, J. Adsorption of gas molecules on monolayer MoS<sub>2</sub> and effect of applied electric field. *Nanoscale Res. Lett.* **2013**, *8*, 425. [[CrossRef](#)]
51. Zhou, C.; Yang, W.; Zhu, H. Mechanism of charge transfer and its impacts on Fermi-level pinning for gas molecules adsorbed on monolayer WS<sub>2</sub>. *J. Chem. Phys.* **2015**, *142*, 1–8. [[CrossRef](#)] [[PubMed](#)]

